



AIAA 2003-0643

**The Interaction of a Synthetic Jet
and a Turbulent Boundary Layer**

Norman W. Schaeffler
NASA Langley Research Center
Hampton, Virginia
United States of America

41st Aerospace Sciences Meeting & Exhibit
January 6–9, 2003
Reno, Nevada

THE INTERACTION OF A SYNTHETIC JET AND A TURBULENT BOUNDARY LAYER

Norman W. Schaeffler*
NASA Langley Research Center
Hampton, Virginia
United States of America

The flowfield resulting from the interaction of a synthetic jet actuator and a quiescent environment and the interaction of synthetic jet actuator and a turbulent, flat-plate, zero pressure gradient boundary layer was examined via stereo particle image velocimetry. Actuators with circular and elliptical orifices were tested and multiple crossflow Mach numbers were investigated.

Introduction

OF all the active flow control actuators currently being studied, there has been a fair bit of attention paid to one particular type of actuator, the synthetic jet. The synthetic jet, simply a deformable cavity connected to an orifice, is identified as being an attractive actuator for a number of reasons. They can be fabricated to a small size, they operate with zero net-mass, i.e., they synthesize a jet-like flowfield without being supplied by an external source of fluid. Therefore, no external plumbing is required to be routed to the actuator simplifying their installation. The jet-like flow created, while zero-net-mass, imparts a finite momentum impulse to the fluid that the jet is synthesized from. Changes in the volume of the cavity either cause flow into the cavity or flow out of the cavity through the orifice. During the outflow phase, a vortex pair, or ring, is formed and moves away from the orifice under the action of self-induction. If the volume of the cavity is changed in a cyclic fashion, a train of vortices are formed, and this vortex train yields, in the mean, velocity profiles similar to that of a turbulent jet.^{1,2}

The majority of the papers, to date, have examined the use of a synthetic jet, or jets, to control some aspect of the flow, the control of separation or circulation, for example. So, attention is drawn to the flowfield as a whole and to the effect that the synthetic jet has on it. In the open literature, one can find the synthetic jet being applied to achieve flow control on a circular cylinder,³⁻⁵ airfoil,⁶⁻¹⁰ and in internal flows.^{11,12} In most of these research efforts, the synthetic jets take the form of a high aspect ratio slot, commonly called a 2-D slot.

The current research effort has the goal of investigating the interaction of a single synthetic jet with a crossflow. So the immediate goal of the effort is not flow control, per se, but gaining understanding of an interaction that plays an important part in active flow control. Therefore, a generic type of synthetic jet and a representative crossflow were chosen. The actuators utilized here have orifices of either a circular or an elliptical cross-section and the turbulent boundary layer over a zero-pressure gradient flat plate, provides the canonical crossflow for them to interact with.

This research effort focuses directly on the events that occur during the operation of a synthetic jet in the neighborhood surrounding the orifice both with and without a crossflow. The motivation for this is to gain understanding into the flow physics involved in the formation of the synthetic jet flowfield and its interaction within a turbulent boundary layer. An increase in our knowledge about this interaction will aid in the development of actuators with increased effectiveness and also will provide data to be used in the development of next-generation design tools to aid in the predication of the performance of flow control actuators.

If we look at the flowfield created by a synthetic jet over a single cycle of its operation, there is a sequence of key events that can be observed. When the volume of the cavity is made to decrease, the synthetic jet is in the exhaust cycle. During this time, fluid begins to flow out of the cavity through the orifice. A boundary layer develops on the walls of the orifice and this boundary layer separates at the end of the orifice. The newly formed free-shear layer then rolls into a vortex ring or, depending on the orifice geometry, a vortex pair. When the vortex ring reaches its maximum strength, based on stroke length and velocity, it begins to move away from the actuator under the action of its own self-induction. After the vortex ring has moved a sufficient distance from the wall, the volume of the cavity begins to expand. The jet has begun its suction cycle. The vortex ring continues to

*Research Scientist, Flow Physics and Control Branch

Copyright © 2003 by the American Institute of Aeronautics and Astronautics, Inc. No copyright is asserted in the United States under Title 17, U.S. Code. The U.S. Government has a royalty-free license to exercise all rights under the copyright claimed herein for Governmental Purposes. All other rights are reserved by the copyright owner.

move away from the exit plane of the actuator and behind the ring, ambient fluid is being drawn in to fill the volume of the expanding cavity. Once the maximum cavity volume is reached, the cycle is ready to begin anew. This cycle is repeated, exhaust, ring formation, ring translation, suction, over and over again typically in a range from 100 to 2000 times a second. The highly directive nature of the exhaust cycle and the sink-like nature of the suction cycle, give the mean, time-averaged, flowfield the appearance of a turbulent jet.

The interaction of a turbulent jet with a crossflow has been studied extensively experimental and computationally. The steady jet injected normally to a crossflow establishes the baseline for these types of flow. In the steady case, the jet is observed to transition as it develops in the streamwise direction from an orientation normal to the crossflow to being aligned with the crossflow. During this process the jet column transforms into a pair of counter-rotating vortices.¹³ This is an easily observed phenomenon. On a windy day, the counter-rotating vortex pair is easily seen on any smokestack. Additionally, there are other vortical structures near the jet exit that exist due to the interaction of the crossflow boundary layer and the orifice.¹⁴ The vorticity contained in the crossflow boundary layer is reorganized by its interaction with the jet, forming a number of structures in the wake of the jet, ranging from horseshoe vortex-like structures to vortices that connect the jet to the boundary layer along the wall.¹⁵ Adding an unsteady component to the jet, by some modulation of the jet velocity, increases the penetration of the jet into the crossflow¹⁶ and introduces some nomenclature for describing the degree of unsteadiness in the jet. Modulation on top of a mean flow creates the pulsed jet,¹⁶ turning the jet completely on and off yields a fully modulated pulsed jet,¹⁷ decreasing the frequency causes the formation of discrete vortex rings¹⁸ and finally increasing the frequency and adding a suction cycle yields the zero-net-mass flux synthetic jet.^{19–22} For active flow control problems, it has been reported that by pitching and skewing the axis of a pulsed jet, with respect to the crossflow, the strength of the spanwise vortices generated by the jet can be increased over the normal injection case.²³ This reduces the “cost” of using an added mass jet for flow control by requiring less mass flow. It is common in all of these studies to have a jet velocity to crossflow velocity ratio on the order of 3 or higher. This is significantly higher than any velocity ratio that will be studied here.

Experimental Program

This research effort was conducted in the NASA Langley 15-inch Low Speed Wind Tunnel of the Flow Physics and Control Branch. This tunnel is a closed-

return atmospheric facility dedicated to basic flow physics research efforts. The tunnel has a maximum speed of 115 ft/sec. During this research effort, the tunnel was equipped with a suspended flat plate model that acts a splitter plate. The plate features an elliptical leading edge. Immediately downstream of the transition from the leading edge to the plate, there is a grit strip to trip the boundary layer of the plate and also grit strips on the tunnel walls at corresponding locations. The ceiling of this tunnel is adjustable at several locations down the length of the tunnel. These supports were adjusted to create a zero pressure gradient over the plate starting from a station 20 inches downstream from the leading edge to a station 50 inches downstream from the leading edge. Flow visualization conducted in this tunnel suggests that the flow is two-dimensional in the zero pressure gradient region of the plate, with the exception of the region close to the wall.¹²

The plate is utilized in this research effort as a false floor. The synthetic jet actuators were fabricated in plug-like modules that were installed into the bottom of the plate so that the upper surface of the actuator plug is flush with the plate. An installed actuator, type C1-B, and the flat plate can be seen in Figure 1. A row of static pressure taps were installed in the vicinity of the actuator plug with a total of 10 taps upstream and 26 taps downstream of the actuator. All of these taps are located on the centerline of the plate. The taps were connected via short lengths of flexible Tygon tubing to an ESP scanning pressure transducer with a full scale range of ± 10 inches of water. The ESP module was located inside the plate model. The module was automatically calibrated at regular intervals during a given test day. The pressure data was used to calculate the freestream velocity over the plate and to verify that the pressure gradient over the plate, in the area of interest, was zero. The presence of the plate increases the top speed in the test section of the tunnel to 145 ft/sec.

The velocity measurements presented here were carried out with a stereo digital particle image velocimetry (SDPIV) system. The timing control, image acquisition, data management and post-processing of the SDPIV data was handled by a commercial system. The light source utilized was a pulsed, frequency-doubled 300 mJ Nd-YAG laser operating at 10 Hz. The flow within the tunnel was seeded with atomized mineral oil with a typical particle size of 5-10 microns. The seed was injected into the flow in the tunnel settling chamber. Standard sheet-forming optics were utilized and the cameras were positioned on the same side of the tunnel. The camera mounts allow for the required tilting of the lens, relative to the camera body, in order to satisfy the Scheimpflug condition. The light sheet was oriented along the centerline

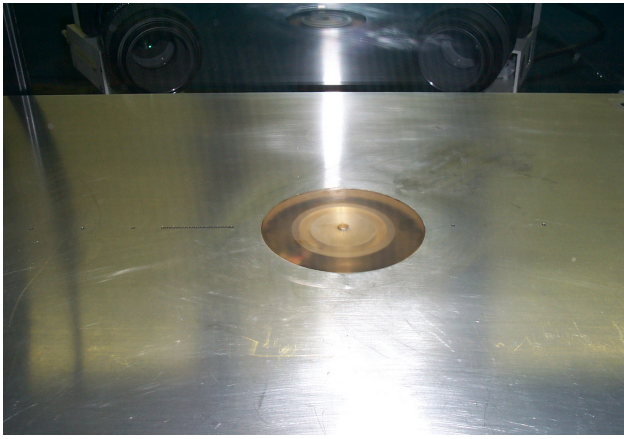


Fig. 1 Actuator C1-B, the circular orifice, installed in tunnel. Camera placement can be seen in the background. The light sheet was located on the centerline of the tunnel, where the static pressure taps are located.

plane of the tunnel along the same line as the pressure taps. This was accomplished through the use of a prism, mounted inside the tunnel far downstream of the actuator. The light sheet thickness was typically 1 mm thick. Both cameras utilized had a resolution of 1008 x 1018 pixels and the typical field of view was 18 mm x 18 mm.

The image acquisition and lasers were synchronized with the drive signal of the synthetic jet so that images could be acquired at a specific time delay after the beginning of a period of the actuator drive signal. We will adopt the nomenclature that a specific delay corresponds to a specific phase of the actuator drive cycle. The drive signal for the actuator was generated on the first channel of an arbitrary function generator and then fed through an audio amplifier before being delivered to the actuator. The start of a period was defined as a zero crossing from negative to positive voltage of the actuator drive signal. The second channel of the function generator was used to generate a square wave that acted as the trigger for the data acquisition. Within the data acquisition software, a timing delay was varied in order to acquire data at 36 specific phases of the synthetic jet actuator drive signal. The flowfield over the entire drive signal, both the exhaust and suction cycles, was recorded as 3600 instantaneous velocity fields, 100 velocity field measurements at each of 36 specific delays. These delays were equally spaced within the drive cycle and resulted in the measurement of the velocity field every 10 degrees of phase. The 100 image pairs were acquired over a period of 10 seconds and were processed using a standard particle image velocimetry (PIV) cross-correlation data reduction technique and then averaged to give the phase-averaged, or ensemble-averaged, velocity field. These phase-averaged velocity fields can then be ordered in time and the evolution of

the jet-induced velocity field, and its interaction with the crossflow, can be studied.

A PIV integration region of 24x24 pixels was used with a overlap ratio of 50%. Due to the nature of the SDPIV technique, only the portion of light sheet that is imaged by both cameras is used in the analysis. It is from this available overlapping image, that an analysis grid is chosen. This results in a typical grid size of 41x72 vectors for the cases without crossflow and 70x53 vectors for the cases with crossflow. Based on the camera resolution and position, lens, and overlap used, there is about 250 microns spacing between the velocity vectors in the full velocity vector maps. Apart from the validation of the velocity vectors during the PIV data reduction, there has not been any other smoothing of the experimental data.

Actuator Design

The two actuators that were utilized in this research effort share the same basic design, differing only in their orifice geometry. Both actuators were driven by a sinusoidal voltage signal with an amplitude of $42 V_{rms}$. The first actuator is equipped with a circular orifice with diameter of 0.189 inches (4.80 mm). This actuator is referred to as C1-B. The second actuator was equipped with an elliptical orifice with major diameter of 0.327 inches (8.31 mm) and minor diameter of 0.109 inches (2.77 mm). This actuator is referred to as E1-B. Both of these geometries yield the same cross-sectional area at the exit, namely 0.028 square inches. Both of these actuators feature a smooth contraction through the top plate of the actuator to the final exit dimensions. Both actuators were produced using stereo-lithography and are made of epoxy. Each actuator use a single piezoceramic driven diaphragm as the active element. The diaphragm is constructed of a circular piezoceramic bonded to a brass shim 50 mm in diameter. The diaphragm is node-mounted, meaning that the diaphragm is bonded to a concentric stage with a diameter of 60% of the shim diameter and the diaphragm is oriented parallel to the exit plane of the orifice of the jet. The cross-section of the circular actuator, C1-B, can be seen in in Figure 2, which illustrates the actuator geometry, its diaphragm orientation and node mounting.

For this style of actuator, the maximum output is realized when the diaphragm displacement is at a maximum. This occurs when the brass shim is excited by the piezoceramic element into one of its structural resonance modes. In order to find the maximum output of the actuators, a hot wire anemometer was used to measure the velocity on the centerline of the jet, 0.1 inches above the actuator surface as a function of frequency. The actuator was provided with a sinusoidal voltage signal, which was $42 V_{rms}$, the same level to be utilized in the experiment. The frequency that yielded

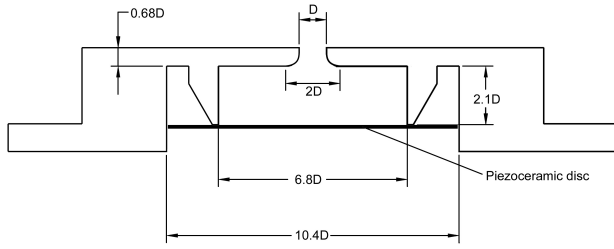


Fig. 2 Cross-section of the C1-B showing node mounting and dimensional details. Actuator mounts through the false floor so that the top surface is flush with the floor.

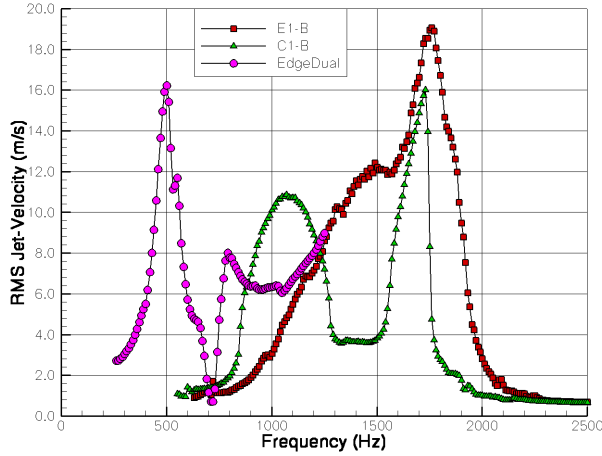


Fig. 3 Frequency Response of the Actuators used in this Research Effort

the highest output for the actuator was subsequently used in the experiment. The frequency response of each of the actuators can be seen in Figure 3 along with the frequency response of a typical slot synthetic jet actuator. For both configurations, we will use as the reference velocity for the jet, the maximum observed root-mean-square (rms) of the jet velocity, as measured on the centerline of the jet, over a complete cycle, and 0.1 inch (2.54 mm) off the actuator surface in a quiescent environment. For the circular actuator, C1-B, the reference velocity, U_j , is 16.2 m/s at a operating frequency of 1730 Hertz. For the elliptic actuator, E1-B, the reference velocity, U_j , is 19.1 m/s at a frequency of 1760 Hertz. In all cases, distances for flows involving the C1-B actuator are non-dimensionalized by the orifice diameter. Distances for flows involving the E1-B actuator are non-dimensionalized by the minor diameter of the orifice, since in all cases examined here the minor diameter is oriented in the streamwise direction.

The Mean Velocity Fields

Before turning our attention to the cases with cross-flow, the case of a jet issuing onto a quiescent environment was examined, both to validate the experimental setup and to identify key features to examine in the

crossflow case.

In Figure 4, the velocity vectors and the some representative sectional streamlines for the case of C1-B actuator operating in quiescent flow are presented. The jet-like nature of the flow is evident from the far field velocity profiles. Only every third row of measured vectors is plotted in this case to aid in the clarity of the figure. All of the velocity fields presented in this paper will be “under-plotted” like this to aid in the clarity of the figure. The amount of the reduction will be noted in the figure caption.

For the case of E1-B, the elliptic orifice actuator, operating in a quiescent flow, the mean velocity field and sectional streamlines are presented in Figure 5. There is an immediate contrast in the two streamline patterns. The flowfield created by E1-B shows an expanding velocity profile as the flow develops in the streamwise direction. The jet grows, just as a turbulent jet grows, by the entrainment of ambient fluid. The flowfield strongly resembles the streamlines generated by a common 2-D slot orifice synthetic jet, such as that illustrated in Figure 14 in Schaeffler, et. al.²⁴ The flowfield created by the C1-B actuator also shows jet-like velocity profiles in the far field, however an interesting feature appears in the near field, namely a standing vortex ring in the mean flow. This standing ring has been observed by other workers,^{25,26} most notably Mallinson et. al.,²⁵ who noted that the standing ring appears to act as a convergent-divergent nozzle, accelerating the mean centerline flow through the ring, reaching a maximum at the center of the ring, then decaying. Analysis of the phase-averaged velocity field will yield a another perspective on the origin of this mean flow feature.

For the crossflow cases, the state of the turbulent boundary layer was documented, with an actuator installed but not running. The observed boundary layer height, height at which $u = U_{99\%}$, and integral parameters for the boundary layers are given in Table 1.

We now turn our attention to the case of the C1-B actuator operating in a crossflow. For a freestream Mach number of 0.050, the mean flow velocity vectors and sectional streamlines are shown in Figure 6. We will accept the displacement of the streamline closest to the wall as a measure of the effectiveness, or authority, of the actuator. It can be seen that the streamline is lifted a significant distance away from the wall. The

	M = 0.05	M = 0.10	M = 0.134
δ	9.59 mm	9.28 mm	8.76 mm
δ^*	1.81 mm	1.75 mm	1.73 mm
θ	1.19 mm	1.18 mm	1.17 mm
H	1.52	1.48	1.47

Table 1 Boundary Layer parameters for the three Mach numbers utilized.

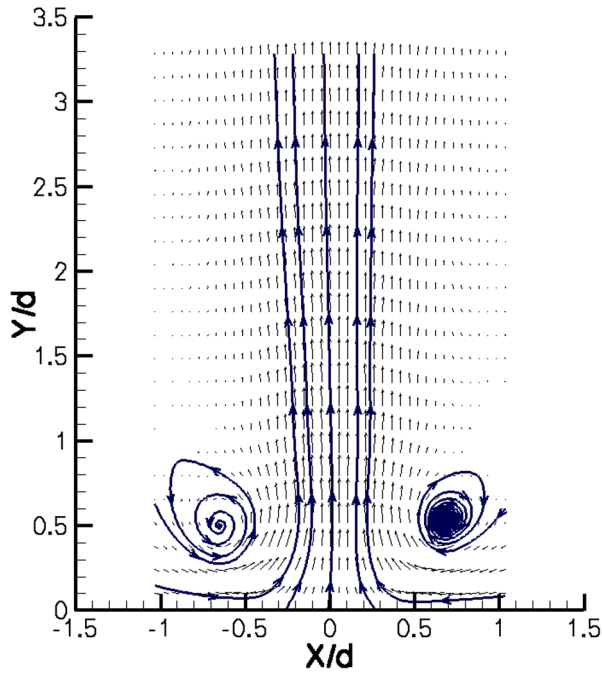


Fig. 4 Velocity Vector map for the C1-B actuator operating in a quiescent environment. Only every third vertical row of data is plotted for clarity.

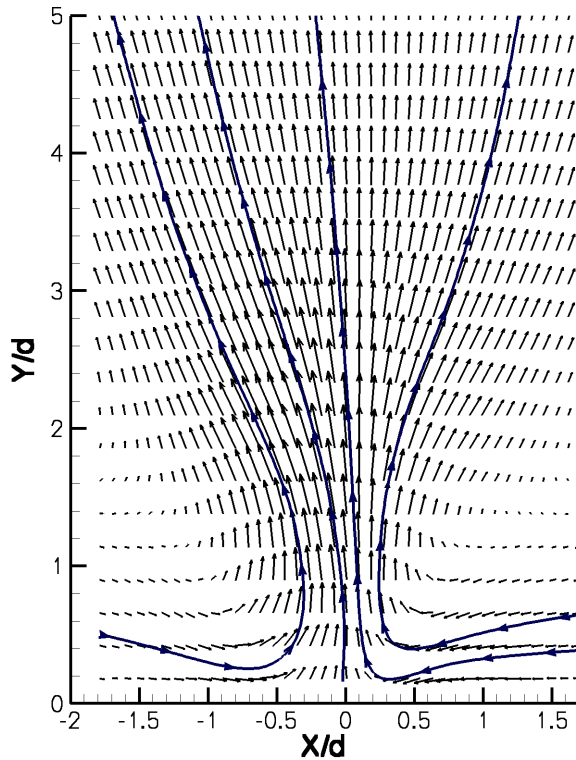


Fig. 5 Velocity Vector map for the E1-B actuator operating in a quiescent environment. Only every third row of data is plotted for clarity.

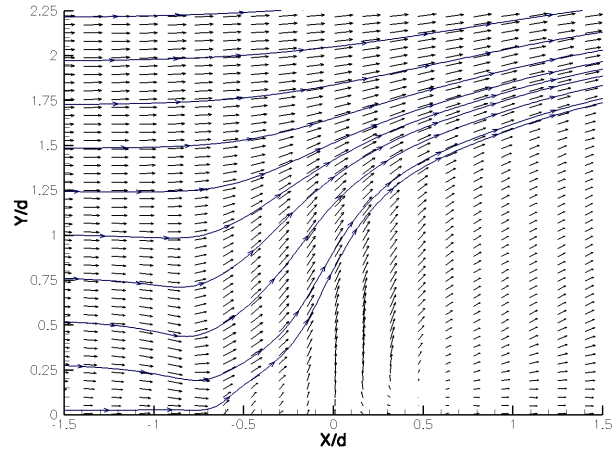


Fig. 6 Velocity Vector map for the C1-B actuator operating in crossflow at $M=0.05$. Only every other column of data is plotted for clarity.

distance that the streamline is lifted, at the edge of the data presented, $x/d = 1.5$, is $y/d = 1.75$ or 88% of the undisturbed boundary layer height. The effect of the actuator gives the impression of creating a separated region of flow. This authority is reduced when the freestream Mach number is increased to 0.100. The mean flow velocity vectors and sectional streamlines for this case are presented in Figure 7. In the figure it is clear to see that the amount that the streamline of interest is lifted away from the wall is reduced, but not by half as might be suggested by the change in velocity ratio. The jet is now able to lift the streamline to about 60% of the undisturbed boundary layer height. Also the inflection points in the shape of our streamline of interest has relaxed to the point of almost disappearing. Increasing the freestream Mach number to 0.134, flattens the shape of the displaced streamline even more, but does not totally eliminate the presence of the inflection points. The displacement of the streamline is further reduced to 44% of the undisturbed boundary layer height. The mean flow velocity vectors and sectional streamlines are illustrated in Figure 8.

We now consider the case of the elliptical jet, the E1-B actuator. The elliptical vortex ring that is expected to be generated by this device is known to be not as stable a vortical structure as the circular vortex ring generated by the C1-B actuator. Elliptical jets and rings are subject to unequal strain rates due to their elliptical geometry and are known to undergo axis switching, the major axis of the vortex ring contracts and becomes the minor axis and the minor axis correspondingly grows and becomes the major axis.²⁷ This process is repeated as the jet develops. It appears that this type of action reduces the ability of the E1-B actuator to displace our streamline of interest. The mean flow velocity vectors and sectional streamlines for the E1-B actuator operating in a crossflow with

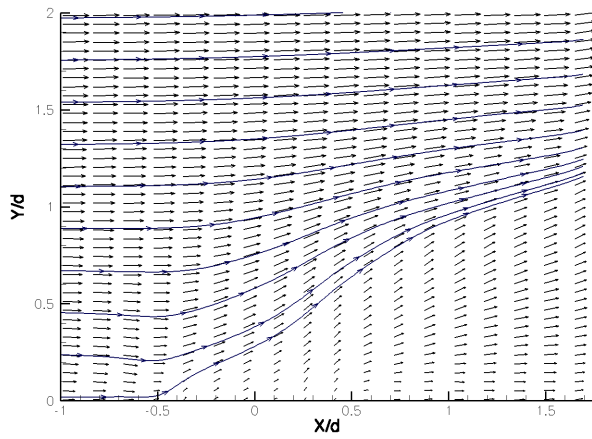


Fig. 7 Velocity Vector map for the C1-B actuator operating in crossflow at $M=0.100$. Only every other column of data is plotted for clarity.

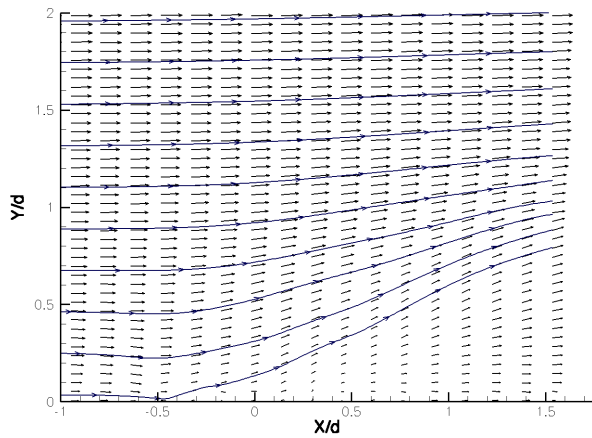


Fig. 8 Velocity Vector map for the C1-B actuator operating in crossflow at $M=0.134$. Only every other column of data is plotted for clarity.

a freestream Mach number of 0.05 are shown in Figure 9. The reference length is now the minor diameter of the elliptic orifice, so the y/d displacement appears higher than the C1-B actuator at similar conditions. However, relating the displacement to the undisturbed boundary layer height reveals that the displacement is only 72% of the undisturbed boundary layer height. This is less than the penetration of the C1-B actuator at the same freestream Mach number, even though the velocity ratio, U_j/U_∞ , for the elliptical synthetic jet is higher than the circular synthetic jet. The shape of the displaced streamline takes on is different from the C1-B actuator. Increasing the freestream Mach number has the same effect on the E1-B actuator as it does on the C1-B actuator, namely a reduction in the distance of penetration. The mean flow velocity vectors and sectional streamlines for this case are illustrated in Figure 10 and the height of the displaced streamline is about 44% of the undisturbed boundary layer

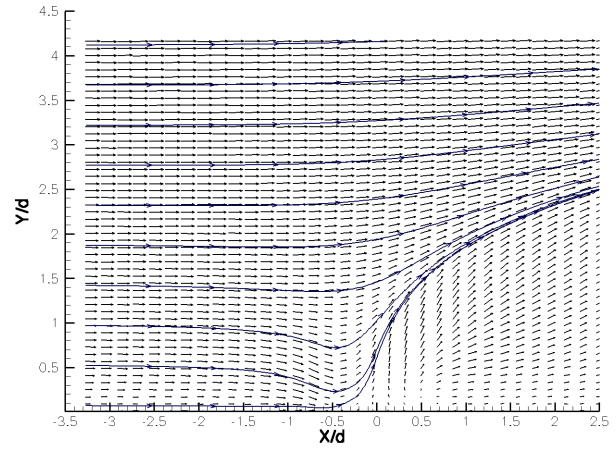


Fig. 9 Velocity Vector map for the E1-B actuator operating in crossflow at $M=0.05$. Only every other column of data is plotted for clarity.

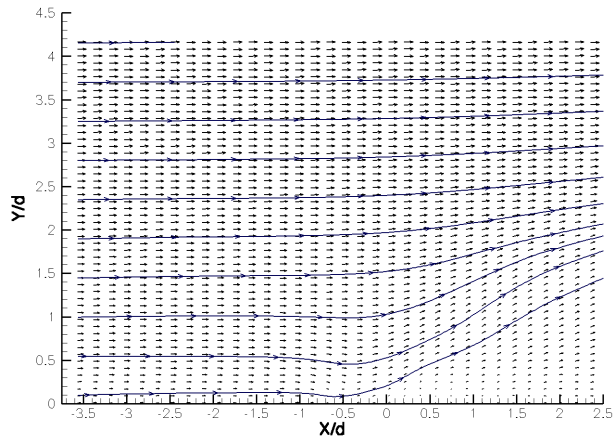


Fig. 10 Velocity Vector map for the E1-B actuator operating in crossflow at $M=0.10$. Only every other column of data is plotted for clarity.

Actuator	M	U_j/U_∞	y/d	y/δ
C1-B	0.05	0.95	1.75	0.88
C1-B	0.10	0.48	1.16	0.60
C1-B	0.134	0.36	0.80	0.44
E1-B	0.05	1.13	2.50	0.72
E1-B	0.10	0.56	1.47	0.44

Table 2 Summary of the mean flow penetration for the crossflow cases studied.

height. A summary of all of these cases is tabulated in Table 2.

The Phase-Averaged Velocity Field

The study of the phase, or ensemble, averaged velocity field allows us to study the evolution of the synthetic jet essentially as a function of time. The 100 instantaneous velocity field measurements, each with their own individual random fluctuations, when ensemble

averaged, yield the typical flowfield at that particular phase, ψ , of the actuator drive signal. All 36 such averages, sequenced in order, document the evolution in time of a typical pulse of the jet over one complete cycle of the actuator.

In Figure 11, the velocity profiles right outside the exit of the jet, measured at a height of $y/d = 0.10$ for the quiescent case and for two different crossflow Mach numbers are presented. The shape and trends of the velocity profiles show a qualitative agreement to the jet exit profiles from the simulations of Mittal,²¹ especially with respect to the distortion of the velocity profile caused by the crossflow when compared to the quiescent flow case.

Interaction with Quiescent Environment

There are still a few things that can be learned from the analysis of the the flowfield generated by the C1-B issuing into a quiescent environment. Inspired by the flow visualizations of the formation process for a circular vortex ring in the paper by Auerbach,²⁸ a post-processing visualization scheme for the experimental data was developed that allowed a number of massless particles to be convected through the measured velocity fields. This allows the motion of the particles to be followed as the jet runs through one complete cycle and then optionally through additional cycles. This visualization scheme was programmed as a network for OpenDX.²⁹ OpenDX is an open source, general purpose visualization package, which is based on the released source code of the IBM Data Explorer software package. Using OpenDX, a set of particles were selected and their displacement recorded as the velocity field changed as a function of time. The velocity field was interpolated between phases as needed to insure a smooth and accurate particle path. If the particle is allowed to convect from the start of the jet cycle to the end, a pathline is traced out on the measurement plane of the velocity vectors. An example of a set of such pathlines can be seen in Figure 12.

Figure 12 requires some guidelines for interpretation. What is being presented are sectional pathlines. Even though all three components of velocity were measured, all of the data still lies only on a single plane. Therefore, the particles are being artificially constrained to remain on that plane, only the in-plane velocity components contribute to the displayed displacement of the particle. Even with this restriction, this technique can yield useful information. Consider, for example, Figure 13, which illustrates an entire cycle of the operation of the jet. Here, instead of plotting lines, like in the case of Figure 12, only the position of the particles at that time are plotted. As time is advanced, the particles then move along their respective pathlines. It can be seen immediately that the ring has just completed forming and has begun

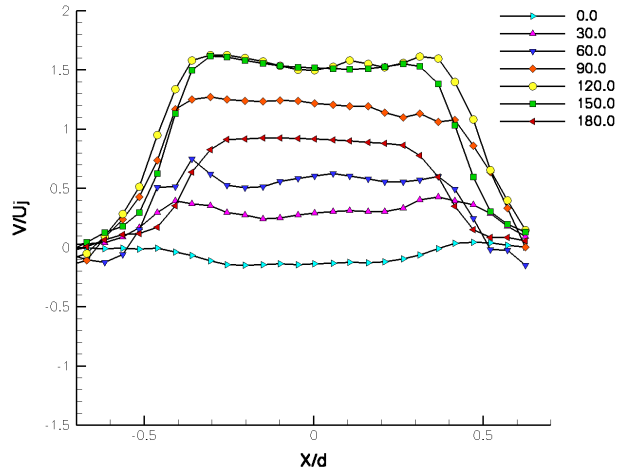
to move away from the wall as the cycle ends. The non-dimensional parameter describing this behavior is the Strouhal number, $St = fd/U$. For the results presented here the orifice diameter, the rms of the jet velocity and the frequency of excitation are used to construct the Strouhal number. For the case of Figure 13, the actuator C1-B, operating at a frequency of 1730 Hz and a jet velocity of 16.2 m/s, then the resulting Strouhal number, St , is 0.51.

Figure 13 illustrates that for this jet velocity and operating frequency, the vortex ring does not complete its development and move away from the wall before the suction cycle begins, as would ideally be the case. For this actuator, the ring interacts with the suction cycle of the actuator and remains close to the wall during the entire actuator cycle. It is the formation of the next pulse from the actuator that will “push” this ring away from the wall. The presence of the vortex ring near the wall for a large part of the actuator cycle is what gives rise to the existence of the standing vortex ring in the mean flow pattern discussed earlier.

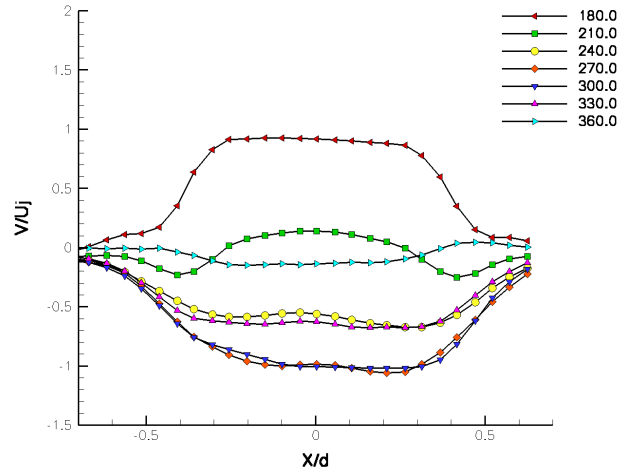
The interaction of the vortex ring and the suction cycle can be plainly seen in the bottom row of images in Figure 13. There it can be seen that the ring diameter actually contracts and this is due to the suction cycle and can be seen in greater detail in Figure 14. The ring contraction can be attributed to two events occurring within the flow.

The first of these events is the two competing demands being placed on the ambient flow, for fluid to be entrained into the ring structure and for fluid to fill the expanding cavity. Auerbach,²⁸ in describing the non-self-similar behavior of the starting vortex in the context of a vortex ring, discusses the mechanism by which the shear layers which will form the ring, first draws distant ambient fluid towards itself by induction and then drags this fluid along by virtue of viscosity. This fluid is entrained into the vortex ring structure and contributes to its growth. Thus, in general, a vortex ring is comprised of fluid that was originally in the shear layer that generated the ring and also of entrained ambient fluid from the environment in which the ring developed. A vortex ring generated by the synthetic jet can be expected to be comprised of the shear layers developed along the orifice walls during the exhaust cycle and an amount of entrained ambient fluid.

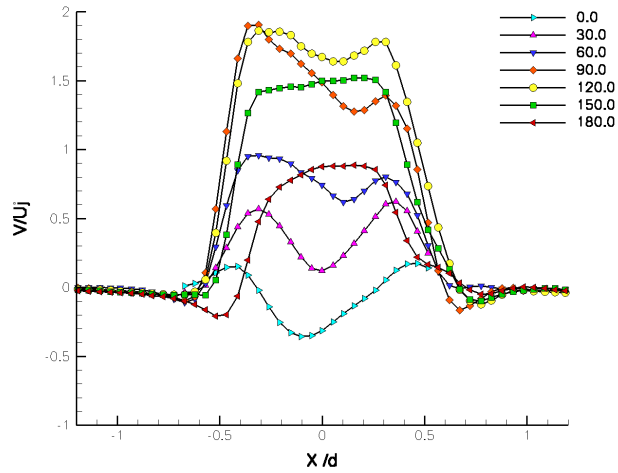
As the suction cycle begins, a demand develops for ambient fluid to fill the expanding cavity of the jet. The two areas of the flowfield that supply the ambient fluid to satisfy each of these requirements must be separate from each other. Thus it is expected that there should be a saddle in the sectional streamline pattern, separating the two zones topologically.³⁰ The existence of a saddle in the sectional streamline pattern was mentioned by Smith and Glezer,^{1,2} but not in the context



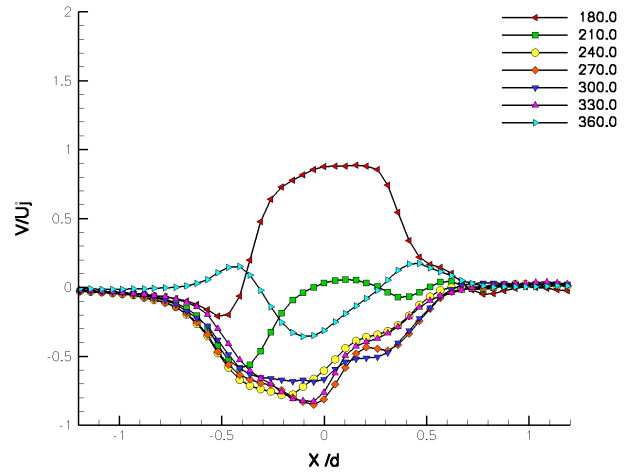
a) $M = 0.00, 0^\circ \leq \psi \leq 180^\circ$



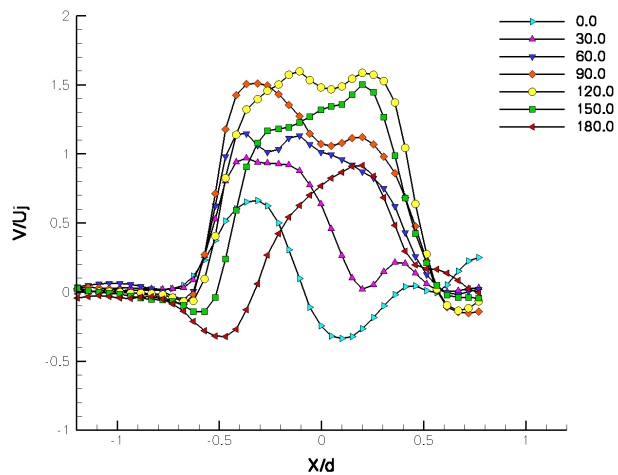
b) $M = 0.00, 180^\circ \leq \psi \leq 360^\circ$



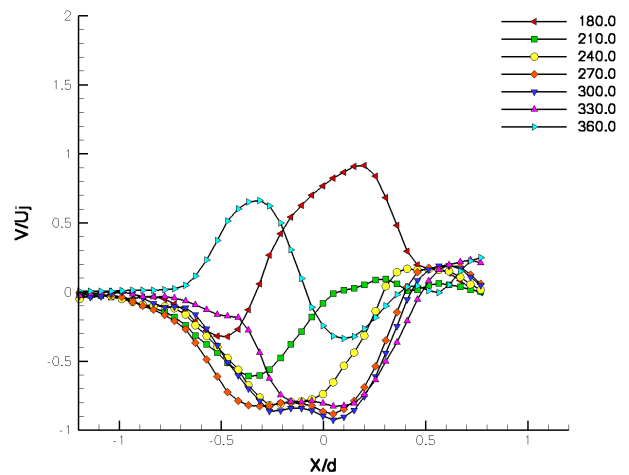
c) $M = 0.05, 0^\circ \leq \psi \leq 180^\circ$



d) $M = 0.05, 180^\circ \leq \psi \leq 360^\circ$



e) $M = 0.10, 0^\circ \leq \psi \leq 180^\circ$



f) $M = 0.10, 180^\circ \leq \psi \leq 360^\circ$

Fig. 11 Exit Velocity profiles at a height of $y/d = 0.10$ for C1-B for different phases of the drive signal. (a) and (b) Quiescent Flow ($M=0.00$), (c) and (d) Crossflow $M = 0.05$, (e) and (f) Crossflow $M = 0.10$.

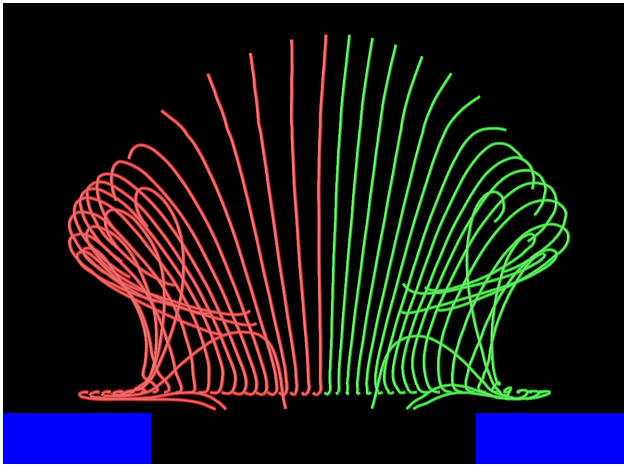


Fig. 12 Sectional pathlines for a complete cycle of the C1-B actuator.

of separating the area of cavity entrainment and vortex ring entrainment. It should be noted that there is no saddle in the mean flow pattern. Figure 15 illustrates the sectional streamline pattern at a phase during the suction cycle. As the cavity fills, ambient fluid that should be drawn into the vortex ring is diverted into the cavity. It is proposed that this limits the growth of the ring to the point that the ring diameter begins to contract in response to the lack of fluid to entrain into the ring structure.

In Figure 16, the variation of the circulation, ring diameter and saddle height as a function of phase angle is presented. The circulation, Γ , was calculated for the right-hand vortex only over the entire right-hand extent of the data and was non-dimensionalized by the circulation of the right-hand vortex in the mean flow pattern, Γ_m . The contour of integration for the circulation is fixed in space as the velocity field progresses through the phases of the jet. The ring diameter, d_v , was also calculated as was the saddle height, S_y . The circulation is seen to grow as the shear layers are ejected and as the ring begins to form. Halfway through the cycle, the circulation is seen to peak in its value at the same time that the contraction of the ring diameter begins to occur. The circulation begins to decay back to the original level as the ring reaches its minimum diameter. This is to be expected, the circulation must vary periodically over a complete phase-averaged cycle. The decay in the circulation must be due to the convection of vorticity out of the field of view. Just as the current ring is contracting, one of the previous rings is being pushed beyond the edge of the measured data. The ring contraction is intimately tied to the displacement of the previous ring by the current ring. For the synthetic jet operating in a quiescent environment, we see that there is a large interaction between each of the ejected rings at this Strouhal number.

The second event taking place in the flowfield that

contributes to the ring contraction continues with this idea that the vortex rings that make up the synthetic jet do not happen in isolation, but instead happen in a cyclic fashion, each ring effecting the next. This effect of each ring pushing the next ring out into the flow is illustrated in Figure 17. Here particle traces from three actuation cycles of the jet and vorticity contours showing the location of the displaced cores can be seen. Each ring wraps its edges around the next ring being ejected, while the main body of the previous ring is pushed out further. The relationship between the newly ejected ring and the previous ring resembles the beginning of the well known process of leap-frogging, but the newly ejected ring does not complete even half of the process. The failure of the process could be attributed to the continual loss of coherence of the previous vortex. Also the vorticity contours reveal an area of opposite signed vorticity between the two rings that may prevent the leap-frogging. This distortion of the previous ring by the newly formed ring contributes to the ring contraction of the newly formed ring.

Crossflow Interaction

There is evidence that the conflict over the entrainment of ambient fluid plays a role to play even in the presence of a crossflow. As we have seen in the mean flow patterns, the C1-B actuator is able to penetrate further into the boundary layer for the case of a $M=0.05$ crossflow than for the case of a $M=0.10$ crossflow. Figure 18 illustrates a set of section streamline patterns for each of these crossflow Mach numbers at the same phase angles. In the $M=0.05$ case, the ring and the cavity are able to balance each other to a higher degree than in higher speed, $M=0.10$, case. In the second case, the saddle stays very close to the wall channeling all of the upstream fluid into the orifice and cutting the vortex ring off from this source of entrainable fluid. It has been noted,²¹ that in the presence of a crossflow, the vorticity in the upstream shear layer suffers from cross-inhalation with the vorticity in the boundary layer. This delays the rolling of the upstream portion of the shear layer into a vortex. This reduced strength and delayed development could explain why the the cavity entrainment is able to dominate the ring entrainment. The fact that the ring does not have access to ambient fluid that it can entrain further limits the strength of the ring. Without a robust vortical structure, the synthetic jet has a reduced ability to interact with the crossflow and reduces the depth of its penetration into the boundary layer.

The interaction of successive pulses as seen in the quiescent flow case does not occur here, the crossflow velocity helps to increase the separation between adjacent vortical structures indicating that the scaling velocity in the Strouhal number should be modified to

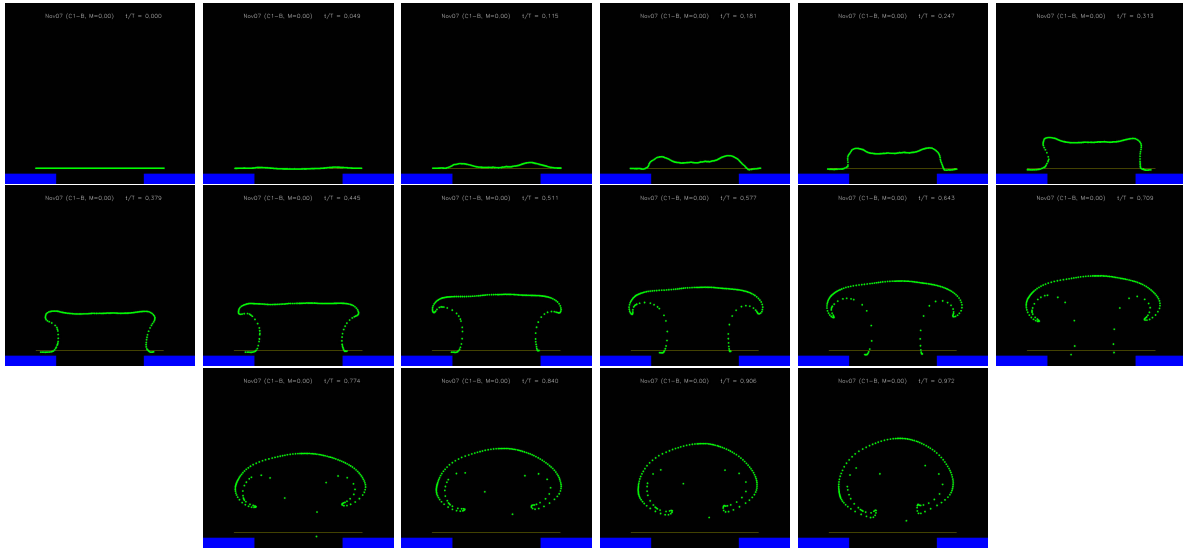


Fig. 13 Particle trajectories based on the measured phase-averaged velocity field, as the actuator C1-B moves through one cycle. No crossflow, Quiescent case, $f = 1730$ Hz.

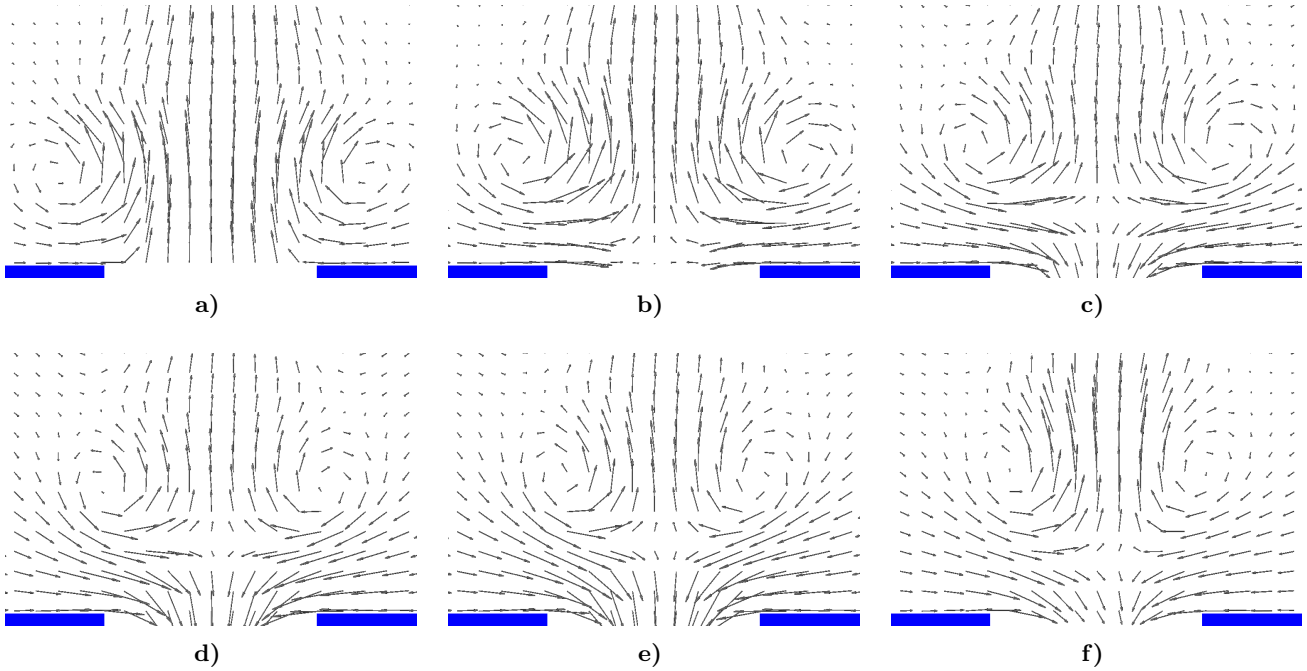


Fig. 14 Velocity vectors based on the measured phase-averaged velocity field, as the actuator C1-B moves through its suction cycle. No crossflow, $f = 1730$ Hz.

account for the effect of the crossflow velocity. In Figure 19, particle locations for two successive pulses and the mean streamline pattern are presented. The two pulses follow the trajectory of the mean streamlines by varying the amount of tilt in the vortex ring as it develops out into the crossflow.

The massless particle convection analysis of the experimental data utilized earlier can also be applied to the case where the flow interacts with a turbulent boundary layer. Figure 20 shows the results of such an analysis. Here particles are launched on four lines, normal to the wall, 1 mm ($x/d = -0.71$) upstream of the jet exit (colored red), at the upstream (yellow) and

downstream edge (blue) of the jet and across the exit of the jet (green), parallel to the wall. As the interaction develops, it is observed that vortex ring, marked by the green particles, is able to entrain a considerable amount of the near wall fluid from upstream and carry these particles a significant distance away from the wall. The ring forms early in the jet cycle and as a result entrains fluid near the wall. In addition, there is a significant effect on the velocity profile downstream of the jet. The field of view in the images of Figure 20 is 10 mm from the wall, the boundary layer height in this area is about 9.6 mm. The convergence of the upstream line of particles to the particles at the edge of the jet is an artifact of

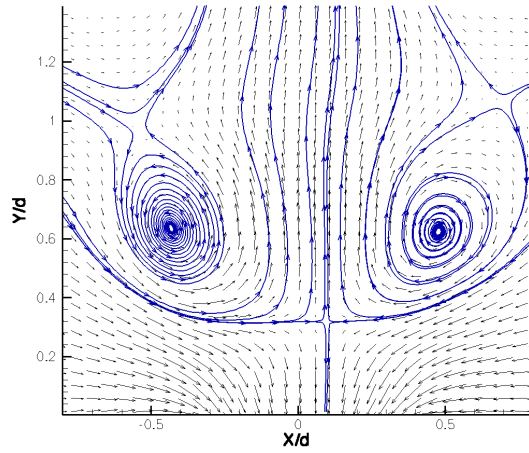


Fig. 15 Streamlines for the C1-B actuator during the suction cycle. Phase angle is 320° . The saddle divides the structures competing for ambient fluid, the vortex ring and the expanding cavity.

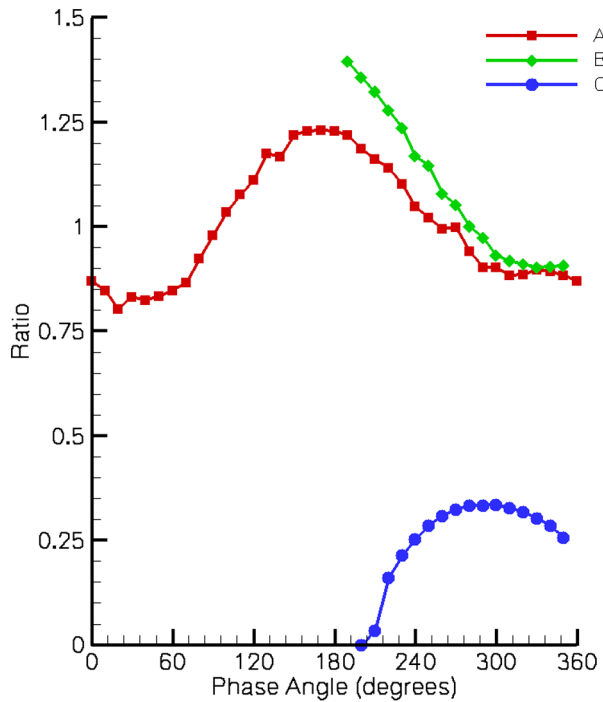
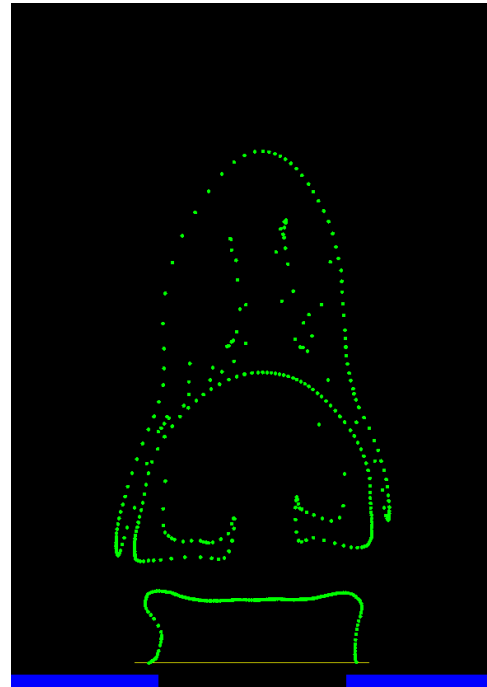
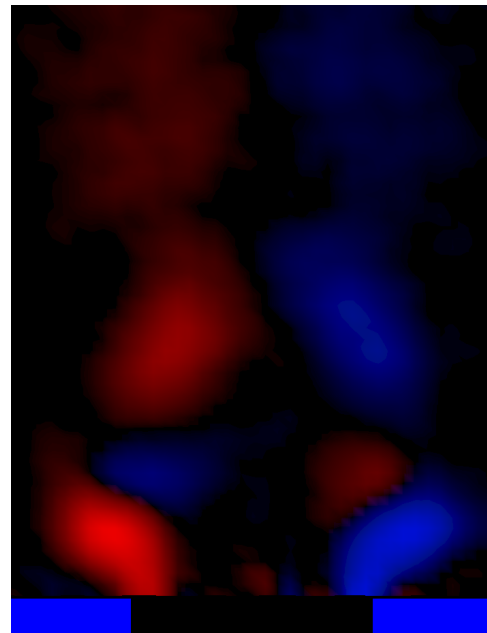


Fig. 16 Circulation, ring diameter, and saddle location as a function of phase for the case of C1-B issuing into a quiescent environment. Ratio A: Γ/Γ_m , Ratio B: d_v/d , and Ratio C: S_y/d

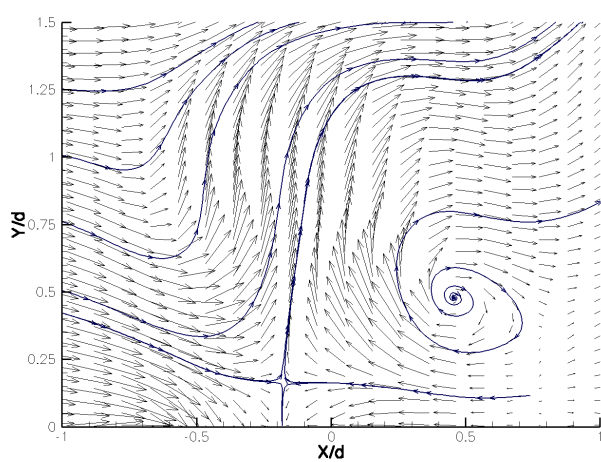


a) Particle Locations after three actuation cycles

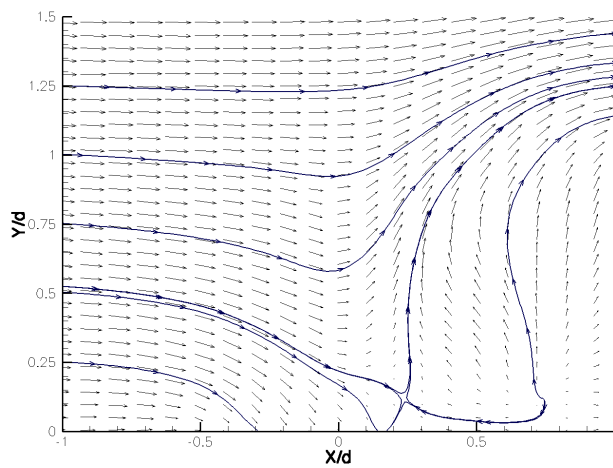


b) Vorticity Contours

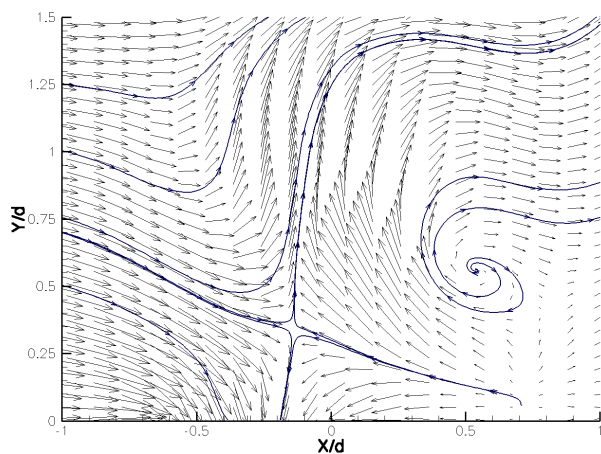
Fig. 17 Multiple cycles of the C1-B actuator issuing into a quiescent flow. Currently a third of the way into the third cycle.



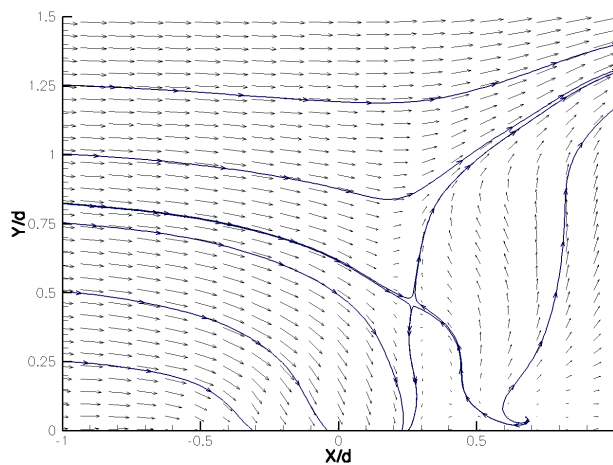
a) $M=0.05$, $\psi = 220^\circ$



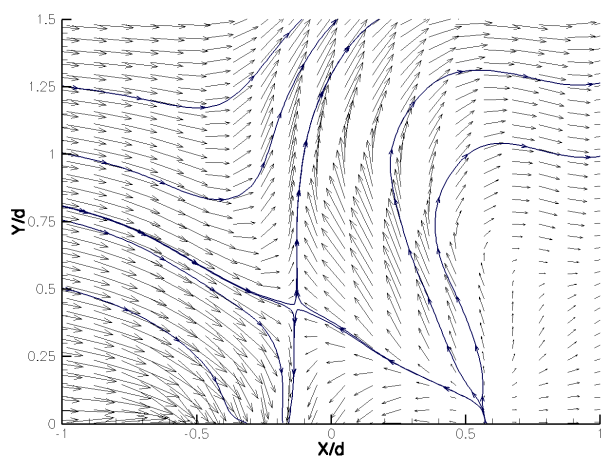
b) $M=0.10$, $\psi = 220^\circ$



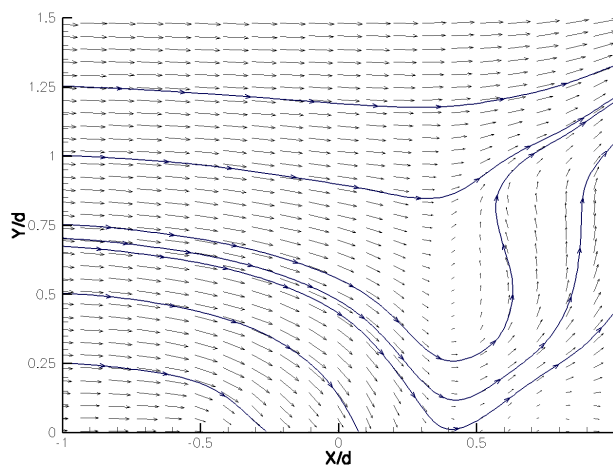
c) $M=0.05$, $\psi = 260^\circ$



d) $M=0.10$, $\psi = 260^\circ$



e) $M=0.05$, $\psi = 300^\circ$



f) $M=0.10$, $\psi = 300^\circ$

Fig. 18 Sectional streamline patterns illustrating the saddle location above the actuator.

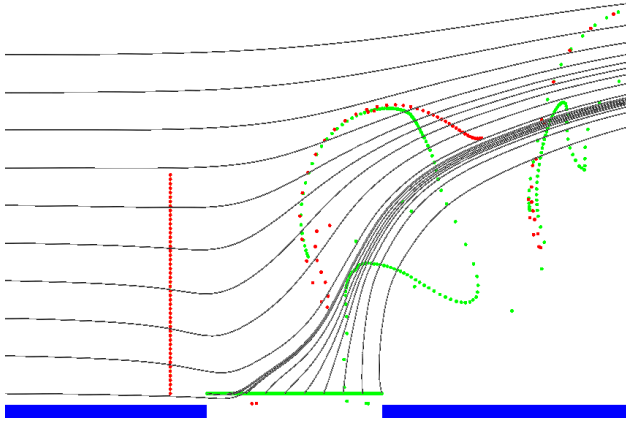


Fig. 19 Particle locations and mean streamlines for multiple realizations of the actuator cycle.

the velocity-displacement constraint discussed earlier. It is expected that the particles would, in actuality, move around the jet, out of the plane, as the upstream flow encounters the jet. The upstream line of particles would need to be moved upstream to $x/d = -1.0$ for the particles to no longer converge on to the particles marking the upstream edge of the jet.

When the crossflow Mach number is increased to 0.10, a robust ring structure is no longer seen to form early in the cycle. This is illustrated in Figure 21, which is constructed using the same set of lines as Figure 20, although the scale of the images are different. Here the pulse is seen to enter the crossflow as a “slug” of fluid, without any initial ring formation. The pulse does not effect the upstream particles significantly until about one third of the way through the cycle. There is no displacement of the particles near the wall out into the outer flow as was seen in the $M = 0.05$ case. There is some evidence that a weakened vortex ring does form after this point, but the mixing accomplished by the ring takes place far from the wall. It is not observed that the movement of particles away from the wall, and the corresponding movement of particles towards the wall, is occurring during the cycle. Overall, the interaction is not as strong as the previous case, reinforcing what was seen in the mean flow.

Conclusions

The interaction of a synthetic jet, with either a circular or an elliptical orifice, with a quiescent environment and a crossflow was documented experimentally. For the case of crossflow interaction, it was found that in the mean flow amount of penetration into the boundary layer is reduced as the freestream Mach number increases. A possible explanation for this was suggested as a conflict between cavity entrainment and vortex ring entrainment. A massless particle convection methodology was introduced to illustrate the

interaction of the jet pulses and the boundary layer flow.

The division of the flow into jet fluid and boundary layer fluid is, in the neighborhood of the orifice, an artificial distinction. As the jet pulse develops and moves out into the crossflow, it does not suddenly appear. It evolves in a continuously changing fashion that interacts with the boundary layer fluid continuously. It has been remarked that since the frequency of operation of a synthetic jet is an order of magnitude higher than a characteristic frequency of the boundary layer, that the jet should appear to the boundary layer as a steady feature. While we have seen there is a well defined mean flow, it is also true that a particle on the edge of the boundary layer will translate about two jet diameters for the $M = 0.05$ case. The jet and the boundary layer must interact in an unsteady fashion, neither seeing the other as a steady feature.

Analysis of the mean flow pattern for the case of a circular synthetic jet interacting with a crossflow shows that the interaction is most significant at the highest ratio of jet velocity to crossflow velocity. The jet can penetrate to 88% of the undisturbed boundary layer height at a velocity ratio of 95%. The elliptical jet, even at a higher velocity ratio, does not penetrate as far away from the wall, indicating that velocity ratio is a indicator of actuator authority once the internal details of the actuator are set, but perhaps not as valid when comparing different actuators types. Analysis of the phase-averaged flow field for two of the cases indicate that the creation of a robust vortical structure early in the cycle is necessary to promote the mixing across the height of the boundary layer. Without the formation of such a vortical structure, the pulse exits as a “slug” of fluid that does not promote mixing early in the cycle and as a result does not lift particles from near the wall away from the wall and into the outer portion of the boundary layer.

Acknowledgments

The author would like to gratefully acknowledge the contributions of Susan A. Gorton, Ronald Geouge, Tony Washburn, and William L. Sellers, III, all of NASA Langley, to this research effort. This research effort was supported by the Morphing Project, AVST, Anna-Maria McGowan, Program Manager.

References

- ¹Smith, B. L. and Glezer, A., “The Formation and Evolution of Synthetic Jets,” *Physics of Fluids*, Vol. 10, No. 9, 1998, pp. 2281–2297.
- ²Glezer, A. and Amitay, M., “Synthetic Jets,” *Annual Review of Fluid Mechanics*, No. 34, Annual Reviews, Palo Alto, California, 2002, pp. 503 – 529.
- ³Amitay, M., Honohan, A., , Trautman, M., and Glezer, A., “Modification of the Aerodynamic Characteristics of Bluff Bodies Using Fluidic Actuators,” AIAA Paper 97-2004, 1997.

- ⁴Béra, J. C. and Sunyach, M., "Control of Boundary Layer Separation by Jet Oscillation," AIAA Paper 98-2373, 1998.
- ⁵Wood, N. J., Sadri, A. M., and Crook, A., "Control of Turbulent Flow Separation by Synthetic Jets," AIAA Paper 2000-4331, 2000.
- ⁶Smith, D., Amitay, M., Kibens, V., Parekh, D., and Glezer, A., "Modification of Lifting Body Aerodynamics Using Synthetic Jet Actuators," AIAA Paper 98-0209, 1998.
- ⁷Amitay, M., Kibens, V., Parekh, D., and Glezer, A., "The Dynamics of Flow Reattachment over a thick Airfoil Controlled by Synthetic Jet Actuators," AIAA Paper 99-1001, 1999.
- ⁸Chatlynne, E., Rumigny, N., Amitay, M., and Glezer, A., "Virtual Aero-shaping of a Clark-Y Airfoil Using Synthetic Jet Actuators," AIAA Paper 2001-0732, 2001.
- ⁹Gilarranz, J. L. and Rediniotis, O. K., "Compact, High-Power Synthetic Jet Actuators for Flow Separation Control," AIAA Paper 2001-0737, 2001.
- ¹⁰Amitay, M., Smith, D. R., Kibens, V., Parekh, D. E., and Glezer, A., "Aerodynamic Flow Control over an Unconventional Airfoil Using Synthetic Jet Actuators," *AIAA Journal*, Vol. 39, No. 3, 2001, pp. 361–370.
- ¹¹McCormick, D. C., "Boundary Layer Separation Control with Directed Synthetic Jets," AIAA Paper 2000-0519, 2000.
- ¹²Jenkins, L., Althoff Gorton, S., and Anders, A., "Flow Control Device Evaluation for an Internal Flow with an Adverse Pressure Gradient," AIAA Paper 2002-0266, 2002.
- ¹³Kelso, R. M., Lim, T. T., and Perry, A. E., "An experimental study of round jets in cross-flow," *Journal of Fluid Mechanics*, Vol. 306, 1998, pp. 111–144.
- ¹⁴Kelso, R. M., Lim, T. T., and Perry, A. E., "New experimental observations of vortical motions in traverse jets," *Physics of Fluids*, Vol. 10, No. 9, 1998, pp. 2427–2429.
- ¹⁵Fric, T. F. and Roshko, A., "Vortical structure in the wake of a transverse jet," *Journal of Fluid Mechanics*, Vol. 279, 1994, pp. 1–47.
- ¹⁶Eroglu, A. and Breidenthal, R. E., "Structure, Penetration, and Mixing of Pulsed Jets in Crossflow," *AIAA Journal*, Vol. 39, No. 3, 2001, pp. 417–423.
- ¹⁷Johari, H., Pacheco-Tougas, M., and Hermanson, J. C., "Penetration and Mixing of Fully Modulated Turbulent Jets in Crossflow," *AIAA Journal*, Vol. 37, No. 7, 1999, pp. 842–850.
- ¹⁸Chang, Y. K. and Vakili, A. D., "Dynamics of Vortex Rings in Crossflow," *Physics of Fluids*, Vol. 7, No. 7, 1995, pp. 1583–1597.
- ¹⁹Smith, D. R., "Interaction of a Synthetic Jet with a Cross-flow Boundary Layer," *AIAA Journal*, Vol. 40, No. 11, 2002, pp. 2277–2288.
- ²⁰Sauerwein, S. C. and Vakili, A. D., "An Experimental Study of Zero-Mass Jets in Crossflow," AIAA Paper 99-0668, 1999.
- ²¹Mittal, R., Rampunggoon, P., and Udaykumar, H. S., "Interaction of a Synthetic Jet with a Flat Plate Boundary Layer," AIAA Paper 2001-2773, 2001.
- ²²Mittal, R. and Rampunggoon, P., "On the virtual aeroshaping effect of synthetic jets," *Physics of Fluids*, Vol. 14, No. 4, 2002, pp. 1533–1536.
- ²³Johari, H. and Rixon, G. S., "Evolution of a Pulsed Vortex Generator Jet in a Turbulent Boundary Layer," AIAA Paper 2002-2834, 2002.
- ²⁴Schaeffler, N. W., Hepner, T. E., Jones, G. S., and Kegerise, M. A., "Overview of Active Flow Control Actuator Development at NASA Langley Research Center," AIAA Paper 2002-3159, 2002.
- ²⁵Mallinson, S. G., Hong, G., and Reizes, J. A., "Some Characteristics of Synthetic Jets," AIAA Paper 99-3651, 1999.
- ²⁶Cater, J. E. and Soria, J., "The evolution of round zero-net-mass-flux jets," *Journal of Fluid Mechanics*, Vol. 472, 2002, pp. 167–200.
- ²⁷Ho, C. and Gutmark, E., "Vortex Induction and Mass Entrainment in a Small-Aspect-Ratio Elliptic Jet," *Journal of Fluid Mechanics*, Vol. 179, 1987, pp. 383–405.
- ²⁸Auerbach, D., "Experiments on the trajectory and circulation of the starting vortex," *Journal of Fluid Mechanics*, Vol. 183, 1987, pp. 185–198.
- ²⁹OpenDX, *OpenDX Visualization Software Package, Version 4.2.0*, <http://www.opendx.org>, 2002.
- ³⁰Perry, A. E. and Chong, M. S., "A Description of Eddying Motions and Flow Patterns and Flow Patterns Using Critical-Point Concepts," *Annual Review of Fluid Mechanics*, No. 19, Annual Reviews, Palo Alto, California, 1987, pp. 125 – 155.

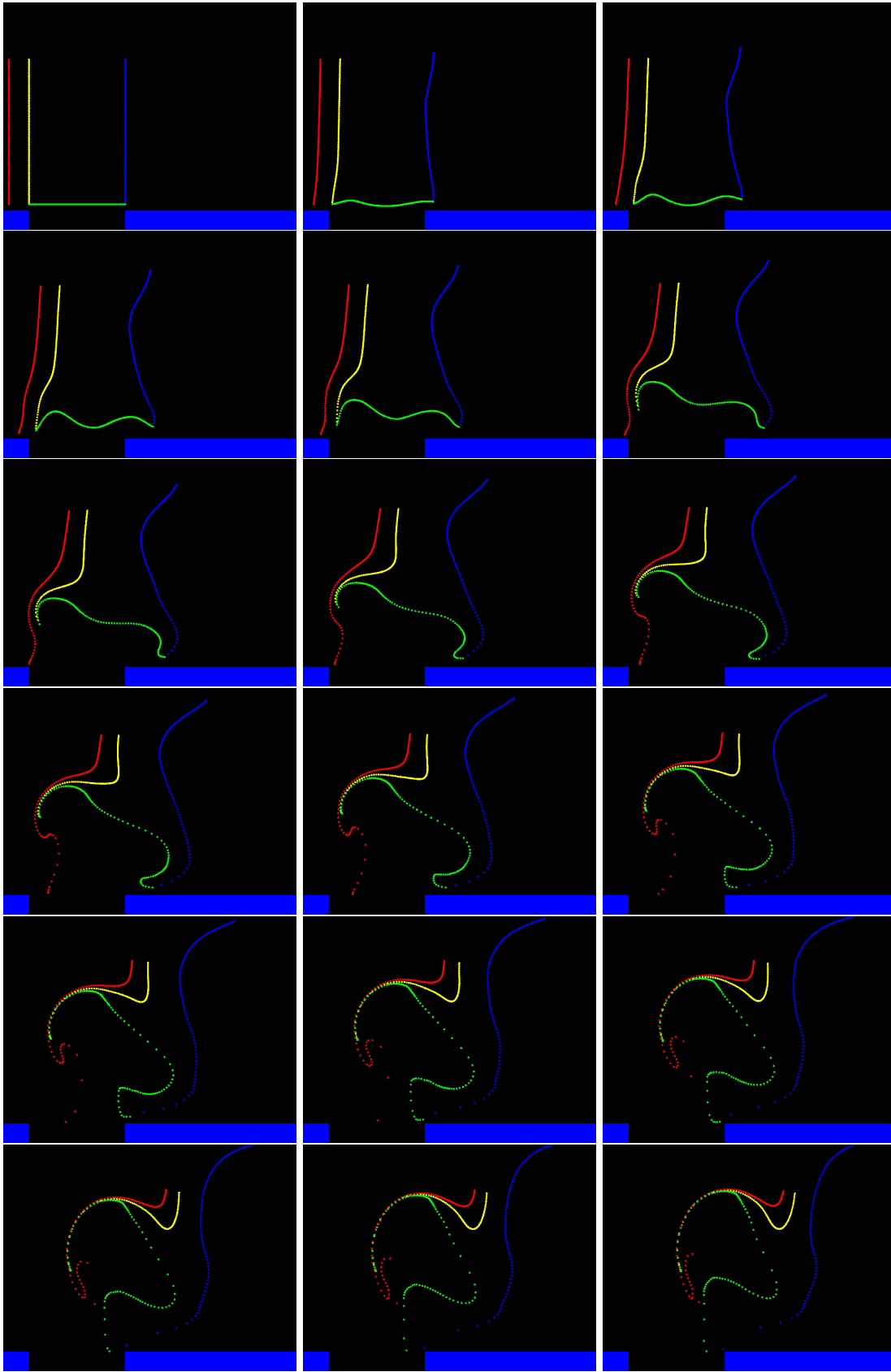


Fig. 20 Particle trajectory analysis based on the measured phase-averaged velocity field. Actuator C1-B. $M = 0.050$, $f = 1730$ Hz. Image height, from wall, is 10.3 mm, $\delta = 9.6$ mm, and the height of the initial positions is 7.5 mm.

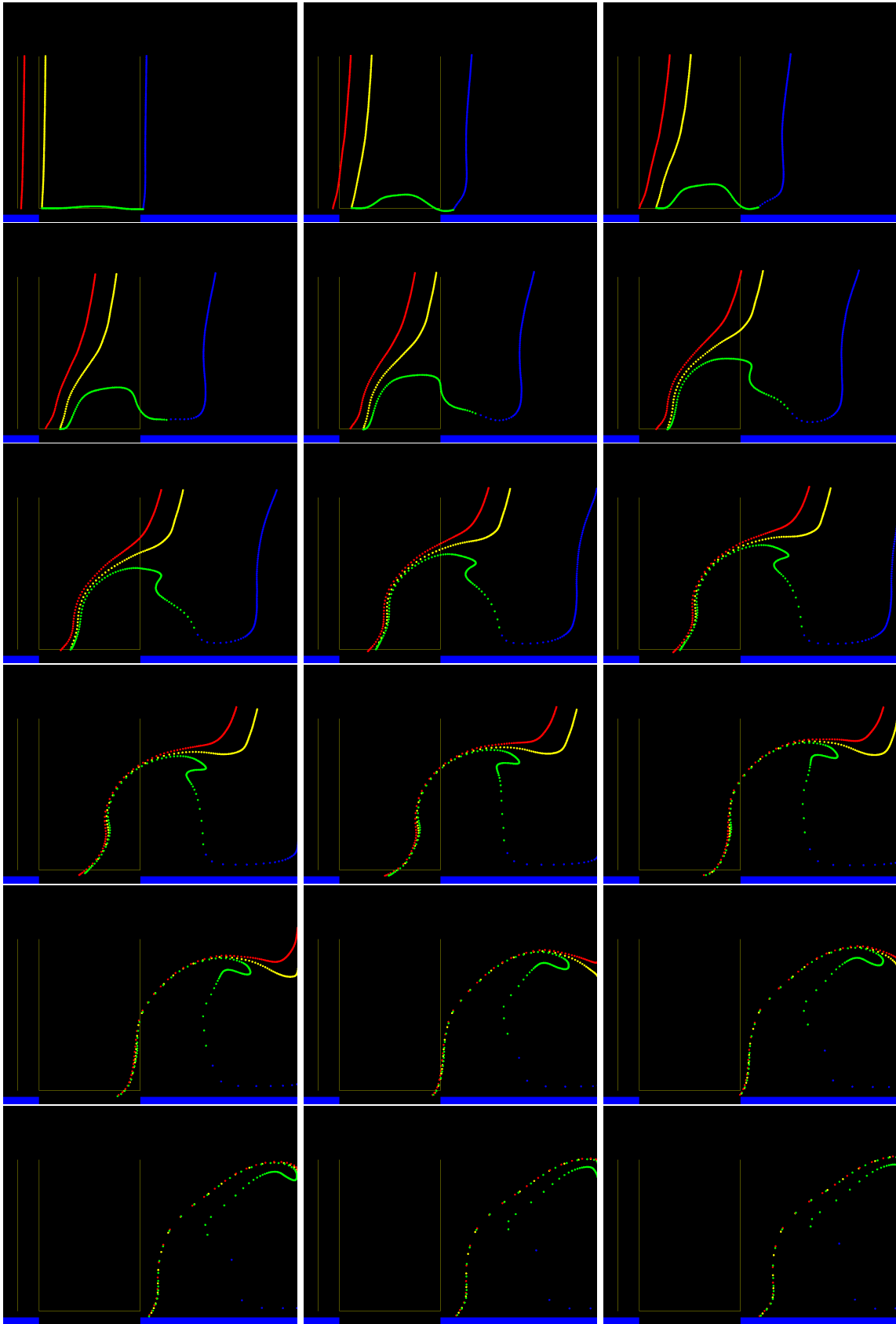


Fig. 21 Particle trajectory analysis based on the measured phase-averaged velocity field. Actuator C1-B. $M = 0.100$, $f = 1730$ Hz. Image height, from wall, is 10 mm, $\delta = 9.28$ mm, and the height of the initial positions is 7.5 mm.